Inside the structure of a nanocomposite electrolyte membrane: how hybrid particles get along with the polymer matrix

Manuel Marechal, F. Niepceron, Gerard Gebel, Hakima Mendil-Jakani, H. Galiano

Journal Name

RSCPublishing

ARTICLE

Inside the Structure of a Nanocomposite Electrolyte Membrane: How Hybrid Particles Get Along with the Polymer Matrix

Cite this: DOI: 10.1039/x0xx00000x

Received ooth January 2012,
Accepted ooth January 2012

DOI: 10.1039/x0xx00000x

www.rsc.org/

M. Maréchal,*[a,b] F. Niepceron,[c,d] G. Gebel,[a,e] H. Mendil-Jakani[a] and H. Galiano[d]

Hybrid materials remain as a target for a fruitful scope of investigations especially for energy devices. A number of hybrid electrolyte membranes consisting of inorganic and organic phases were then synthesized. Mechanical, solvent uptake and ionic transport properties were studied with the key point being the characteristic length scale of the interaction between the phases.

A group of nanocomposite membranes made of polystyrenesulfonic acid-grafted silica particles embedded in a Poly(Vinylidene Fluoride-co-HexaFluoroPropene) (PVdF-HFP) matrix is studied combining neutron and X-ray scatterings on the nanometer to angstrom scale. This approach allows for the variation in morphology and the structure as a function of particle loading to be described. These studies showed that the particles aggregate with increasing particle loading and these aggregates swell, creating a physical interaction with the polymer matrix. Particle loadings lower than 30 wt.% induces a slight strain between both of the subphases namely the polymer matrix and the particles. This strain is decreased with particle loading between 20 and 30 wt.% conjointly with the beginning of proton conduction. Then the percolation of the aggregates is the beginning of the significant increase of the conduction without any strain. This new insight can give information for the variation in other important intrinsic properties.

Introduction

The large family of composite electrolytic polymer membranes has been extensively studied[1-4] with applications from energy devices such as fuel cells to membrane processes. This family can be divided into several subfamilies depending on whether the polymer phase is an ionic conductor and whether the inorganic or hybrid phase contains ionic groups. One of the main families is constituted of membranes with a polymer electrolyte such as Nafion®-like perfluoroalkylsulfonic acid polymers[5-11] and sulfonated polyaromatic polymers.[12, 13] These polymers then include a second phase consisting of either an inorganic filler like mineral (laponite,[7, 12, 14] montmorillonite,[8-10] ZrO_2,[15] SiO_2,[16] calcium hydrophosphonate,[6] TiO_2[9]) or a heteropolyacid (hydrophosphoric acid,[17] orthophosphoric acid,[18, 19] phosphotungstic acid,[15, 20-24] phosphomolybdic acid,[21, 22, 25] silicotungstic acid,[21, 23, 26] phosphoantinomic acid,[27] zirconium phosphate sulfophenyl phosphate,[28] zirconium phosphate,[11, 23] mesoporous acid silicate[12]). The overall objective is to decouple or couple the properties of the obtained membranes depending on the applications These properties are, for example, the improvement of ionic conductivities, the mechanical properties and/or the water retention at elevated temperatures.[11] The inorganic or hybrid fillers can also be embedded in non-ionic polymers, such as partially or perfluorinated polymers.[29, 30] The obtained membranes are known to be chemically and electrochemically stable, with respect to the potential window of the applications.[31]

The assumptions, that the hydrophilic nature of these composite membrane systems create an environment with increased water uptake and increased ionic conductivity (especially at high temperature up to 120°C), are questionable[32] although experimentally supported in the literature by confused and/or contradictory results[9-11]. For example, the improvement of the proton conductivity was low the last 20 years[4, 10-12] by using hybrid membranes in the field of low/medium-temperature fuel cells. In the main family described above constituted of polymer electrolytes and fillers, the different descriptions are not clearly and definitely backed up:[5, 6, 12] (i) The water contained in the particles cannot easily be shared with the rest of the polymer electrolyte phase, and (ii) the conductivity of the inorganic/hybrid phase is in general at least one order lower than the one of the electrolytic organic phases. Nevertheless some

composite membranes have better properties in the application uses.[8, 11] Improving effects of the mechanical properties at the local scale and the localization of the crystalline zones[6] are invoked to explain this paradox. The ionic transport has been shown to be intimately linked with the local mechanical properties[33], the crystallinity of the polymer phases and the multiscale structure.

Many associated properties still remain elusive, such as the sizes, the distribution and the structure of the inorganic or hybrid particles, the interactions and the structure/properties interplays between these subsystems. This questioning is legitimized by recent systems obtained by using the silicon sol-gel chemistry.[4, 34-36] Indeed, it has been possible to locate and to control the inorganic phase (size, structure),[35-37] even at the nanoscale.[38, 39] The control of the ionic inorganic hybrid phase has significantly enabled the ability improve the ionic conductivity in composite membranes. In this study, an original composite membrane composed of conducting polystyrenesulfonic acid-grafted silica particles into a Poly(Vinylidene Fluoride-co-HexaFluoroPropene) (PVdF-HFP) matrix[30] was used to address and clarify these questions.

The structural studies of such hybrid membranes are rare, notably due to the presence of two subsystems. Despite this complexity, the study of multiscale materials using direct (AFM, SEM)† and reciprocal (SAXS/SANS, WAXS)‡ spaces, can permit to reach a thorough structural description.[40, 41] Bulk and surface information is obtained in a large range of characteristic length scales. In the reciprocal space, the size, shape and interface effects can be discriminated between the different subsystems due to the large gaps between the related characteristic correlation lengths. The distribution and the size of the hybrid particles are notably characterisable. The structural variation of the aggregates of particles, the variation of the polymer crystalline phase and their interactions as a function of the loading of hybrid particles were then described.

Experimental (All experiments were performed at room temperature.)

† AFM Atomic Force Microscopy, SEM Scanning Electron Microscopy.

‡ SANS Small Angle Neutron Scattering, SAXS Small Angle X-ray Scattering, WAXS Wide Angle X-ray Scattering.

Composite Membranes N,N-dimethylformamide (DMF, Aldrich, anhydrous, 99.8%) was used as received. A high molecular weight grade of PVdF-HFP copolymer from Solvay (Solef®21508) was used for the preparation of composite membranes.

The polystyrenesulfonic acid-grafted silica particles, referred to as A390-g-PSSNa, were obtained by grafting sodium 4-styrenesulfonate from the surface of fumed silica particles, using atom transfer radical polymerization techniques (Fig. 1).

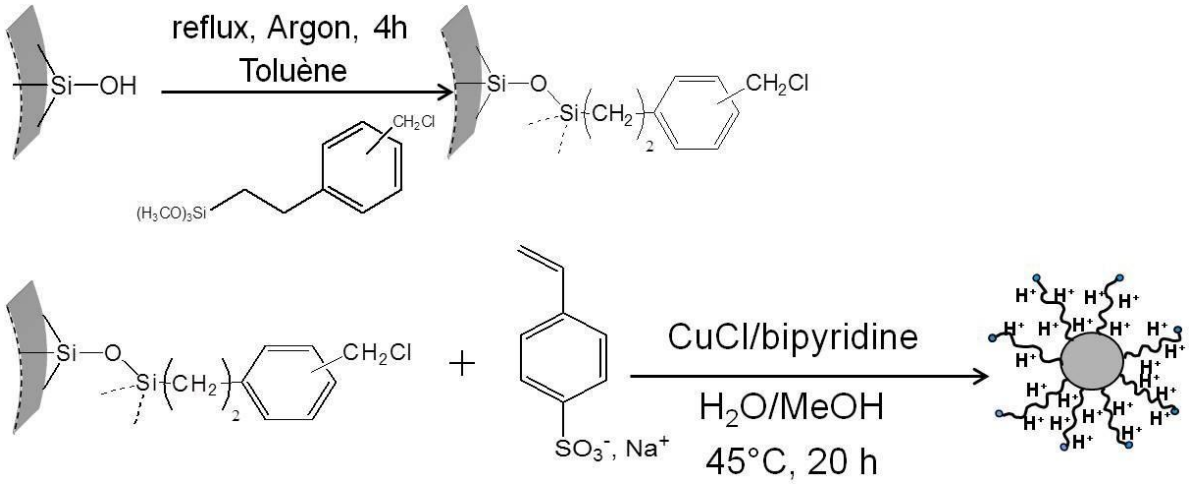

Figure 1. Scheme of the synthetic route for the production of A390-g-PSSNa.

The synthesis of these high proton conducting silica particles has been described in a previous paper (see SI S0-1 for more details and SI S0-2 for the characterization of sizes).[30] The same batch of particles, with an Ionic Exchange Capacity (IEC) equal to 2.7 mequiv./g, was used for preparation of composite membranes.

Composite membranes in the sodium salt form were obtained by solvent evaporation on a glass plate using a laboratory scale hand coater set at 60 °C. Viscous dispersions of A390-g-PSSNa and PVdF-HFP in DMF were obtained by first dispersing a known weight of A390-g-PSSNa in DMF for 48 h before the addition of a known weight of PVDF-HFP. The dispersions were then stirred for 70h before casting, affording composite membranes with loadings ranging from 10 to 70 wt.% (SI Tab. S1). The membranes were removed from the glass plate by immersion in a water bath and then stored under standard conditions.

The hydration state of the membrane is characterized by λ, the number of water molecules per ionic group. The experimental sorption isotherms (SI Fig. S1) were carried out to obtain λ=f(*RH*) knowing the ionic exchange capacities[30] with a dynamic vapour sorption balance. The membranes were then equilibrated with several atmospheres having different water vapour pressures using statured ionic solutions at 25°C. The salts (SI Tab S2) impose a known relative humidity (RH).[42, 43]

Confocal Laser Scanning Microscopy (CLSM) This technique was used in the fluorescence mode. Observations were conducted with a Leica TCS-SP2 (Leica Microsystems Heidelberg, Germany). A water immersion objective lens was used with 0.31 μm as theoretical resolution in the x–y plane. The membranes were labelled with the fluorochrome rhodamine B solution at 5 ppm during 1 minute and washed by immersion in ultrapure water bath. Membranes in hydrated state were inserted between a concave slide and a coverslip and then hermetically sealed. The incident light was emitted by a He/Ne laser beam at 543 nm which exited the rhodamine B. The fluorescence light was recorded between 560 and 700 nm. ImageJ program (free software developed at the National Institutes of Health) was used to obtain 3D building of membranes by Z-stack methodology.

Scanning Electron Microscopy (SEM) was used to investigate the morphology in-plane and of the cross-sections of the acid-form membranes. The surfaces were observed using a field emission gun microscope Zeiss Ultra 55 microscope at 5 kV, in the secondary electron mode. The cross-sections were obtained by fracturing in liquid nitrogen.

Atomic Force Microscopy (AFM) The AFM technique was used in an intermittent-contact mode which is a soft contact mode. The force applied by the tip is constant during the scanning thanks to an electronic control loop. The Nanoscope IV from Digital Instruments with a Dimension 3100 Controller allowed to record two types of signal: the height and the amplitude variations as a function of the scanning position. Both resolutions, lateral and vertical, respectively depend on tip radius and the force (or the amplitude).

Small-Angle X-ray Scattering (SAXS) The measurements were performed at the ESRF (European Synchrotron Radiation Facility, Grenoble, France) on the BM02-D2AM beamline. The incident photon energy was tuned to 12 keV which corresponds to a wavelength of λ=0.103 nm, and the path length was 1 mm. A two-dimensional detector, a CDD camera developed was used. Two different distances between the sample and the detector were used to cover magnitudes of the scattering vector q from 0.07 to 11 nm^{-1}. The intensity curves measured by the long geometry were scaled to the absolute intensities with the aid of a laboratory-calibrated Lupolen® sample. The scattered intensities were recorded during 20 s. The corrections of primary data were carried out. As an additional correction, the contribution of the empty cell was subtracted to the scattering intensity of the studied samples. The membranes were sealed in circular holders equipped with Kapton® windows.

Small-Angle Neutron Scattering (SANS) Small-Angle Neutron Scattering (SANS) experiments were carried on the small angle spectrometer PAXE spectrometer of Léon Brillouin Laboratory (Saclay, France). Two sample-to-detector distances (SDD) and neutron wavelengths (λ) were used to cover magnitudes of the scattering vector modulus q from 0.05 to 4 nm^{-1} (λ=1.2 nm, SDD = 4 m, and λ=0.5 nm, SDD = 1.5 m). The resulting flat level of the scattering intensity at the high q values is of the order of magnitude of the experimental background.

Wide-Angle X-ray Scattering (WAXS) X-Ray diffraction investigations were carried out on a X-Pert Pro MPD Philips diffractometer (cobalt $K_{\alpha 1}$ radiation: λ = 0.1789 nm) using Bragg-Brentano incidence reflection geometry (θ/2θ). The detector was moved by 2θ steps of 0.02°, and the counting time was at least 5 s per step. Soller slits were mounted both in the incident beam path (0.04 rad), and the diffracted beam path (0.04 rad). The divergence slit was automatically adjusted giving a 10 mm irradiated length. The diffractogramms were recorded in the 2θ range going from 5 to 120°. The software Profit (Version 1.0c, Philips Analytical X-Ray) was used to process, and to fit both raw data and ($I \cdot q^2$ vs. q) profiles.

Results and discussion

The homogeneity on the macroscopic scale of the different membranes is the main condition to validate the study. To follow the morphology variation as a function of the particle loading, the ionic domains of the membranes were first labelled with a fluorochrome. The 3D rebuilding was then obtained by using Confocal Laser Scanning Microscopy (CLSM) (Fig. 2)

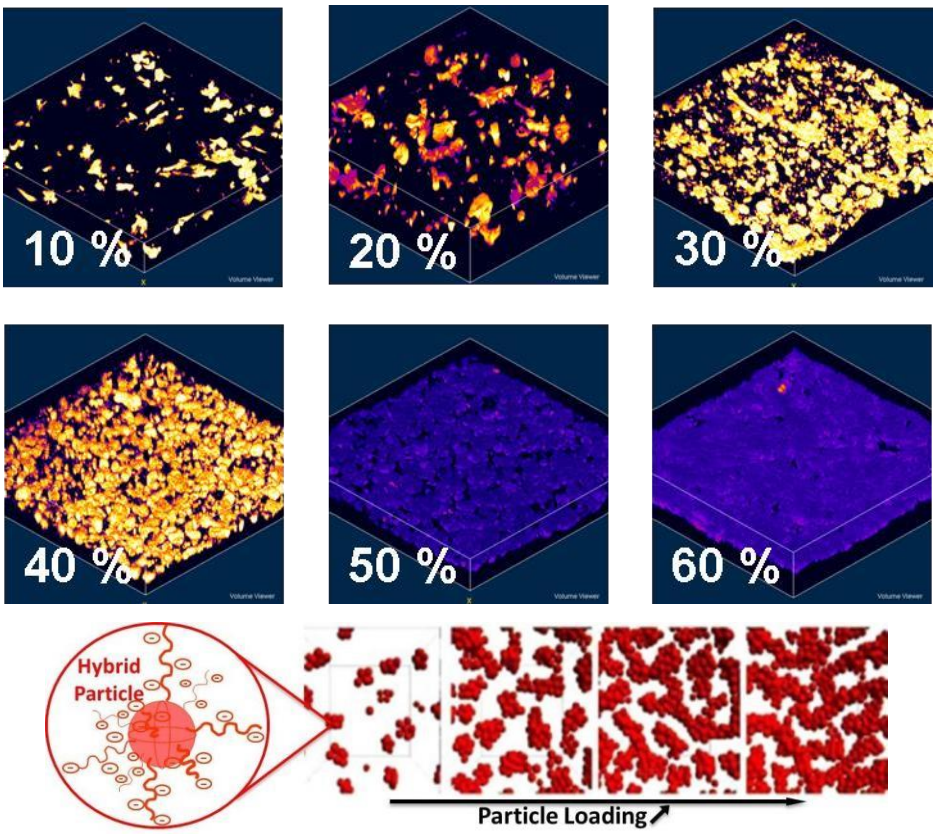

Figure 2. 3D building of membranes by CLSM for several amounts (wt.%) of particles (size: 150 x 150 x 30 µm^3). The aggregates of particles are represented in yellow/orange (10% to 40%) and blue (50% to 60%) in the microscopy images, and in red for the simulations.

This method permits to probe a thickness of 30 µm, i.e. 50 vol.% of the membranes. The results are representative of the whole morphology, i.e. the spatial distribution of the particles and their connectivity, of the samples since they were confirmed by SEM (EDS[§] of Si, F, C, S and Na elements) along the thickness of the membranes, and they are similar for each face.

[§] EDS Energy Dispersive X-ray Spectroscopy.

For a low particle loading, until 20 wt.%, the phase separation is significant due to the incompatibility of both phases being consist of the polymer and the swelled particles. The hydrophilic domains are not well-connected, and increase in size with the loading. For 30 wt.% of particles, the size of the aggregates of particles concomitantly decreases with an increase of their number. These domains are evenly distributed in the volume, and become to be connected which can be considered as the percolation threshold. Above this limit, the material becomes a proton conductor since the proton conductivity starts to significantly increase[30](SI Fig. S2). At higher loadings, co-continuous domains appeared progressively in the volume as a whole. At 50 wt.% of particles, the appearance of porosities defines the transition from a dense material to a porous one. The resulting materials are self-standing membranes composed of interconnected aggregates. The homogeneity of the membranes is then confirmed in a large range of loadings.

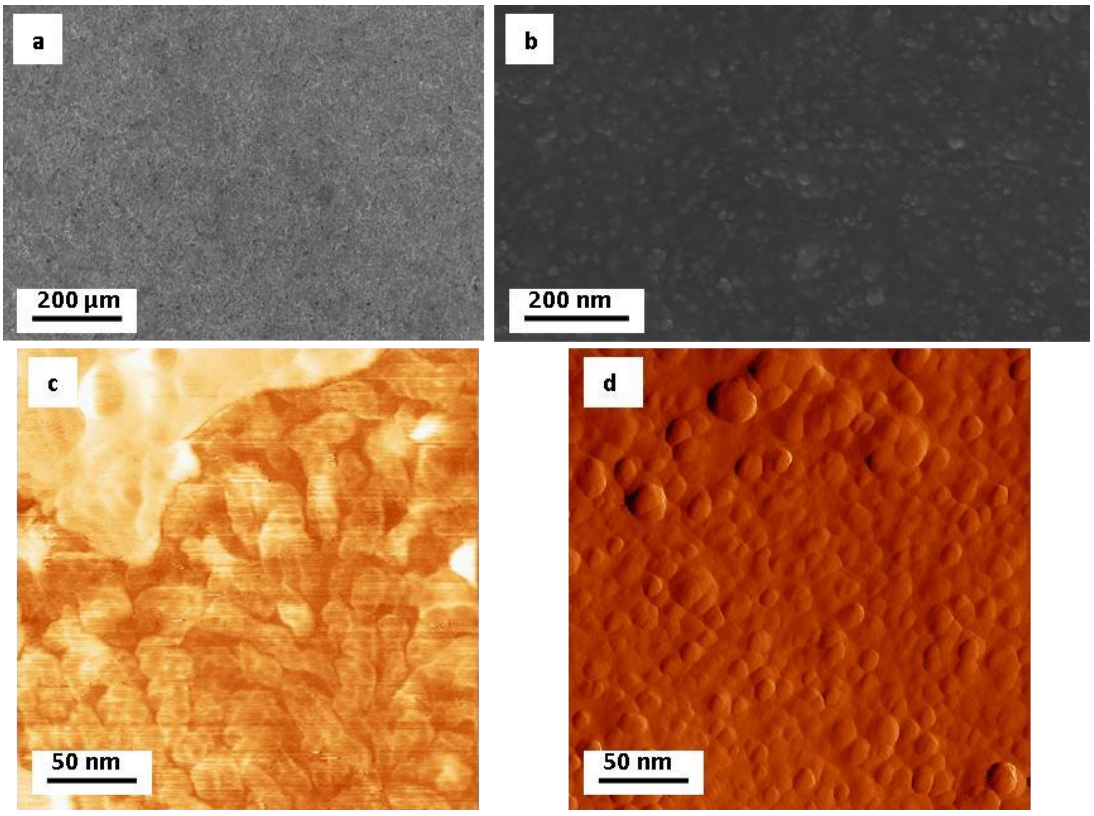

Figure 3. Membranes with 50 wt.% of fillers at 50 %RH: typical SEM micrographs on the surface (**a)**, on the cross-section of the cryofractured membrane **(b)**, on the surface by AFM pictures in phase imaging (**c**) and in error amplitude (**d**).

This observation is also strengthened by SEM and AFM. At the mesoscopic scale with the SEM images (Fig. 3a and 3b), the membranes appear homogeneous. On the micrograph of the surface (Fig. 3a), the holes are due to shadow-particles of the aggregates, and their depths are in the same order of magnitude than their diameters between 50 and 100 nm. The morphology of cross-sections, which were obtained by fracturing membranes in liquid nitrogen, were also investigated by SEM. Figure 3b highlights the presence of aggregates, about few tens to hundred nanometers, embedded in a second phase, which can be attributed to the polymer matrix made up of PVdF-HFP. The AFM images (Fig. 3c and 3d) reveal that the aggregates are formed of sub-aggregates especially thanks to the Figure 3c with an average size around 10 nm above a loading of 30 wt.%. To sum up, (i) the particles merge to form aggregates with the loading, (ii) these aggregates measure between fen tens up to hundred nanometers, and (iii) they concomitantly percolate with the increase of the conductivity (SI Fig. S2). SAXS and SANS were then used to refine the description of this nanoscale distribution. These complementary techniques provide insights into the interfaces, swelling behaviours, multiscale, and multicomponent organisations.

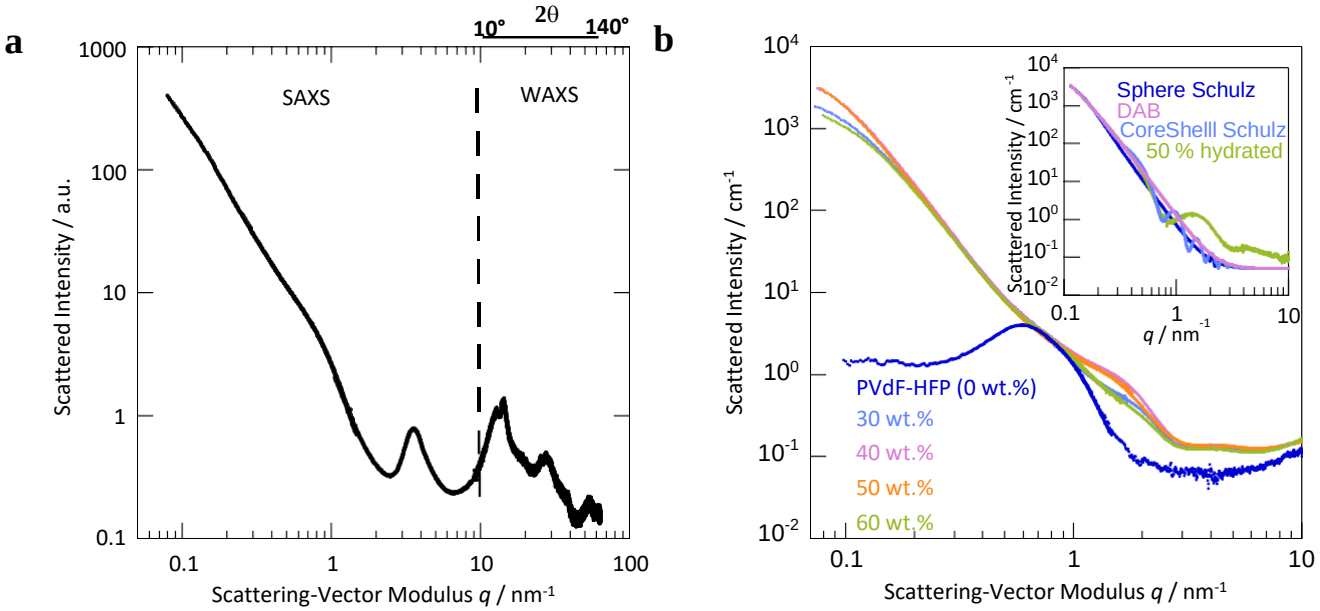

Figure 4. (a) SAXS/WAXS profile at 50 %RH of a membrane with 50 wt.% of fillers, and (**b)** SAXS profile for water swollen membranes at different loadings (wt.%) as a function of the scattering-vector modulus *q*, and (inset) fittings of the form factors of a swelled membrane with 50 wt.% of fillers (i) for core-shell spheres with shell thicknesses distributed according a Schulz distribution, (ii) with the Debye-Anderson-Brumberger scattering model (see SI M1), and (iii) for homogeneous spheres with sizes distributed according to a Schulz distribution (see SI M2).

Indeed scattering techniques are well suited to probe the nanostructure of hybrid membranes characterized by multiphase systems. The related length scales of heterogeneities are then described from the mesoscale to the molecular scale, i.e. the correlation lengths ranging from hundred nanometers to few angstroms (Fig. 4a). These heterogeneities of electron and neutron densities, due to different subsystems and cause of different scattering coupled terms, lead to complex scattering patterns. Indeed the scattered intensities, being the sum of the contributions of the different subphases, with their form and structure factors, make the interpretation complex. A progressive approach was then used ranging from the low to the wide angles of scattering, since the description of the aggregates of particles, through the correlation length between the crystallites of the polymer matrix, the distances between the polyelectrolyte chains, the variation of the crystallites of the polymer matrix for ending the

intramolecular distances of the membranes. This description was possible by dissociating the different contributions with different particle loadings (Fig. 4b), the relative humidities (Fig. 5a), and the contrast variations (Fig. 5b). The neutralization with a cesium salt increases the electronic density contrast between the hydrophilic phase and the ionic groups.

The upturn in intensity at low scattering-vector can be easily attributed to the scattering of the heterogeneous distribution of the aggregates, commonly interpreted as an inhomogeneity at the scale of several hundred nanometers.[44] This conclusion clearly appears in the Figure 4b comparing the hybrid membranes to the PVdF-HFP reference membrane. These multiscale structures can be described, and especially the aggregates made up of hybrid nanoparticles. Moreover, at low *q*, the electronic contrast variation leading to a modification of the shape of the upturn for high relative humidities (Fig. 5a) is due to the form factor variation, i.e. the size and/or the shape of the hybrid particles change, since the low *q* part of the neutron scattering (Fig. 5b) slightly varies with neutron contrast variations. The shape especially changes for the higher relative humidities (Fig. 5a). Then the swelled aggregates slightly break up with the distance between the particles. This variation is concomitant with the divergence of the sorption properties (SI Fig. S1). This swelling at high relative humidities do not exclusively concern the hydrophilic parts of the aggregate, i.e. the polyelectrolyte chains, but also every "refillable" accessible volumes and notably the volume created between the hybrid particles. To sum up, at high relative humidity and especially at high loading, the aggregates overswelled and break up. Below 0.4 nm^{-1}, these upturns (Fig. 4, 5, S3 and S4) are mainly due to the scattering of the hybrid particles within the aggregates. Since the SAXS interpretation is already complex with polymer-grafted nanoparticles in solution[45], the following approach was implemented to describe this complex system in which these particles are embedded in a polymer phase.

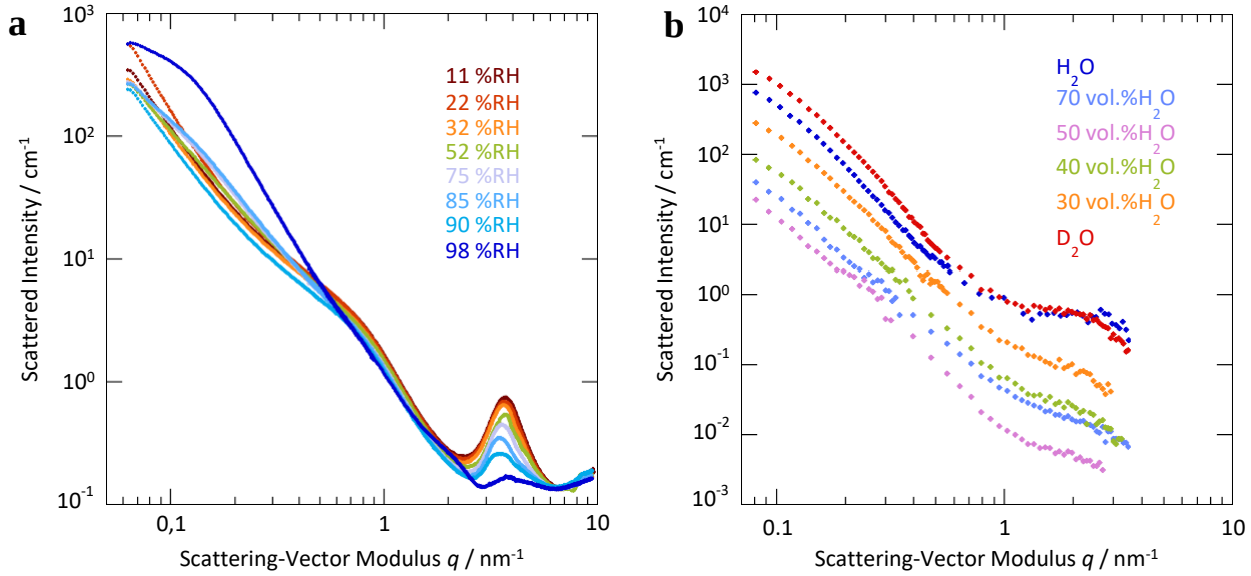

Figure 5. (a) SAXS absolute intensity as a function of the scattering-vector modulus for different swelling states (% of surrounding, and **(b)** Neutron scattering intensities versus scattering-vector modulus for different isotopic solution compositions of a membrane with 50 wt.% of fillers

The approach, after different simulations with the expected shapes, i.e. form factors of overlapped core-shell hybrid spheres, was first to use reasonable and robust solutions by minimizing the number of variables between several and one or two variables at most. These variables are the radii of the core and the shell, their dispersions, and parameters to take into account the overlap of the particles and aggregates. Indeed the interferences stemming from particles interactions, i.e. structure factor effects, are important, and then have to be considered by using relevant models. Different simulations using several form and structure factors support the following choices. These different fittings permitted to conclude, and to choice the relevant models to fit with the same set of parameters all the SAXS data resulting from different samples and conditions, i.e. relative humidities (Fig. 5a), and cation natures (SI Fig. S3 and S4).

Finally the best agreement between the experimental and the simulated scattering curves were obtained with the Debye-Bueche model[46, 47] (see SI M1) by considering the existence of large-

scale fluctuations of the density of the particles. However these results were compared with the local order model with the relevant agreement for the shape and the intensity of the scattering curves, i.e. a sphere model with a continuous distribution function of macroion's size and charges[48, 49] (see SI M2). Both approaches, the Debye-Bueche and the local model, coupled with the contrast variation, by neutralizing with a cesium salt, and the hydration states, i.e. swelled or dried, permitted to improve the fittings in order to significantly reduce the number of adjusting parameters.

The electronic density variation of the ionic phase, with the relative humidity and the cation exchange, allows modulating the density contrasts at the interfaces between the hydrophilic phase and the polymer phase. It is then possible to probe and to discriminate the contrast variations between one or several cores and a hybrid particles or a sub-aggregate of them. Especially for the low loadings, two of them were more precisely evaluated, the silica-core radius and the thicknesses of the polyelectrolyte shells. The variation in the correlation lengths (Tab. 1) globally show the same trend, the average correlation length increases with the loading.

Table 1. Best-fit parameters of the fitting procedure with hybrid membranes in different conditions with the two models, the Debye-Bueche (L_{DAB} is the characteristic correlation length which is a measure of the average spacing between both regions.) and the spherical models (R is the radius of a particle or of compact spherical-like particles of a finite number of particles and σ is the root-mean-square deviation from the mean size.)

Cation Swelling	Loading [wt.%]	L_{DAB} [nm]	R [nm]	σ
H^+ Hydrated	30	9.1	7.9	0.42
	40	10	7.1	0.47
	50	13	6.1	0.58
	60	13	6.7	0.55
Cs^+	30	5.8	5.7	0.56
	40	5.9	6.2	0.38

Dry	50	6.3	6.5	0.34
	60	6.2	6.3	0.35
	30	9.4	8.5	0.40
Cs^+	40	10	7.9	0.45
Hydrated	50	14	9.1	0.47
	60	15	8.2	0.51

The spherical model evaluates a compact aggregate of a finite number of native hybrid particles. Then R, the radius of a particle or of compact spherical-like particles of a finite number of particles with the local model, increases with the loading as $L_{DAB,}$ the characteristic correlation length of the Debye-Bueche model. The electronic densities of PVdF-HFP (d=1.75-1.78 g/cm^3, M_w≈35,0000 g/mol), SiO_2-A390 (d = 2.2 g/cm^3, M = 60.08 g/mol), polystyrenesulfonic acid (d = 1.18 g/cm^3, M_w≈ 40,000 g/mol) and water respectively are 9.0, 6.6, 3.5 and $3.3 \cdot 10^{23}$ e$^-$/cm^3. The electronic density of Cs^+ being estimable to $4.6 \cdot 10^{23}$ e$^-$/cm^3, the electronic density variation with this cation is then not the most significant and relevant in the wet state. The dispersions of R (σ), in both H^+ and Cs^+ forms, increase from 0.40 to 0.55, and R slightly decreases from 8.5 to 6.1 nm. The increase of the dispersion is mainly due to the inclusion of more than one particle in the determination of R. The slight decrease of R can be attributed to the interdigitation of the sulfonated polystyrene shells. In the dried state, the dispersion decreases, and R reaches a plateau at 10 nm. This correlation length is the average radius of one dried hybrid particle. The L_{DAB} in the three different conditions permits to probe the two main isodensities between the silica cores and the hydrophilic phase (polystyrenesulfonic acid + water + Cs^+ or H^+), and between the hydrophilic phase and the PVdF-HFP. The core of the hybrid particles constituting the aggregates can be evaluated at 6 nm and the thickness of the shells at 7 nm. L_{DAB} are of the same order of magnitude than R which is small for large-scale fluctuations. An average density smaller than the electronic density of the shells around a sub-aggregate can explain this agreement. To sum up the characteristic sizes of the particles, (i) the radius of the core and the thickness of the swelled shells are respectively around 6 and 7 nm, (ii) the slight decrease of the radius with the

loading can be attributed at the interdigitation of the shells and the increase in size of the aggregates.

The broad peak obtained for the PVdF-HFP membrane appears in the *q*-range in which the intensity does not change in the nanocomposite membranes, i.e. does not shift in position or in intensity as a function of the loading (Fig. 4b, S3 and S4) or the relative humidity (Fig. 5a). This correlation length is attributed to the distance between the crystallites of the semi-crystalline polymer phase[50, 51] considering a sufficient electronic contrast between the amorphous and the crystalline phases. The intercrystallite distance is well-known to slightly shift with the different conditions and processes.[31] The semi-crystalline polymer phase can be treated as lamellar systems. This model assumes that the SAXS intensity arises from the electron density difference between the lamellae and amorphous layers. It is generally accepted[50, 51] that crystallites are formed in lamellar structures, but this does not mean that the lamella is fully crystalline. On the basis of the position of the lamellar period peak (q^*),[52] the lamellar period (L) is calculated as $L = 2\pi/q^*$. The lamellar period is the sum of the average widths of the lamellae and amorphous layers. In the present case this value is 10 nm, q^* being equal to 0.61 nm^{-1} obtained using a Gaussian model to fit the peak. To sum up, the interlamellar distance is invariant and equal to 10 nm.

The variation in intensity between 1 and 3 nm^{-1} as a function of the loading (Fig. 4b, S3 and S4) can be assigned to the form factor of the hybrid particles. Indeed they can be simulated by a core-shell model (SI Fig. S5) with the parameters obtained in the low-*q* range. The PVdF-HFP phase is embedding the hybrid particles constituted of grafted sulfonated polystyrene chains on silica cores. The contrast variation is a relevant approach since this polyelectrolyte layer or shell around the silica particles swells with water. The main technique is the isotopic replacement.[53, 54] Indeed this method is powerful to describe a complex structure.[55] The swelling solution (100% H_2O) is replaced by a mixture of H_2O and D_2O to find the average scattering cross-section of the hydrophobic phase. This approach permits to probe into the hydrophilic/hydrophobic interfaces, e.g. mainly silica/water, the PVdF-HFP matrix with the water, and between the sulfonated-polystyrene-acid chains in the swelled shells. The

scattering signal extinguishes between 0.8 and 2 nm^{-1} for mixtures about 64 vol.% D_2O, e.g. for neutron scattering length densities (SLD) about $2.76 \cdot 10^{14}$ m^{-2} (Fig. 5b). The theoretical SLD of the PVdF-HFP and the silica particles can be respectively evaluated around $3.15 \cdot 10^{14}$ and $3.47 \cdot 10^{14}$ m^{-2} in the bulk state, the SLD of sulfonated polystyrene chains being between $1.48 \cdot 10^{14}$ and $1.58 \cdot 10^{14}$ m^{-2}. These matching ratios evolving along an average SLD express the intensity extinction of different contributions/interfaces in the different range of *q*, i.e. in the different length scales. The contrast variation permits to reveal a broad peak at 2 nm^{-1}. By comparison with the whole structural description of this system, this peak is interpreted as a very dispersed correlation length due to the interdigitation of the sulfonated polystyrene chains linked to two distinct particles. The average distance between two interdigitated chains is then about 3 nm.

Otherwise the correlation length between two chains belonging to the same hybrid particles can be studied by varying their swelling (Fig. 5a). This method permits to reveal a thinner peak whose intensity decreases with the relative humidity due to the decreasing of the electronic contrast between the chains. The related correlation length does not vary with the swelling since the sulfonated polystyrene chains are covalently bounded on a silica particle. By describing the peak with a Gaussian shaped peak, the average correlation length is found to be equal to 1.71 nm, *q* being equal to 3.67 nm^{-1}, with a small standard variation of 0.07. The dissymmetry is due to the interdigitation contribution. A mean value of 22 chains of sulfonated polystyrene per hybrid particles (close to 0.45/nm^2) is estimated. This order of magnitude is somewhat four times higher than the one obtained by using this grafting-from method to graft polystyrene chains with larger silica particles[45].

This incremental approach therefore allows to simulate the form factor of the hybrid particles with relevant parameters (SI Fig. S5), to isolate the contribution of the polymer matrix (Fig. 4b), and to describe the polyelectrolyte chains (SI Fig. S6). A better understanding of the structure factors could then permit to model the small-angle *q*-range. Nevertheless the results stress the possibility of a dichotomous interpretation leading to an overall quantitative and qualitative description of the nanostructure.

Concomitantly the invariance of the intercrystallite correlation length with the loading questions about the crystallite variation themselves. WAXS measurements permit to evaluate short-range periodicity in a polymer membrane. Thus the WAXS intensities are typical of a semicrystalline polymer. They include the Bragg reflections and a broad peak respectively arising from the crystalline and the amorphous phases. The ratio of the crystalline to amorphous phases can be calculated through a profile analysis.

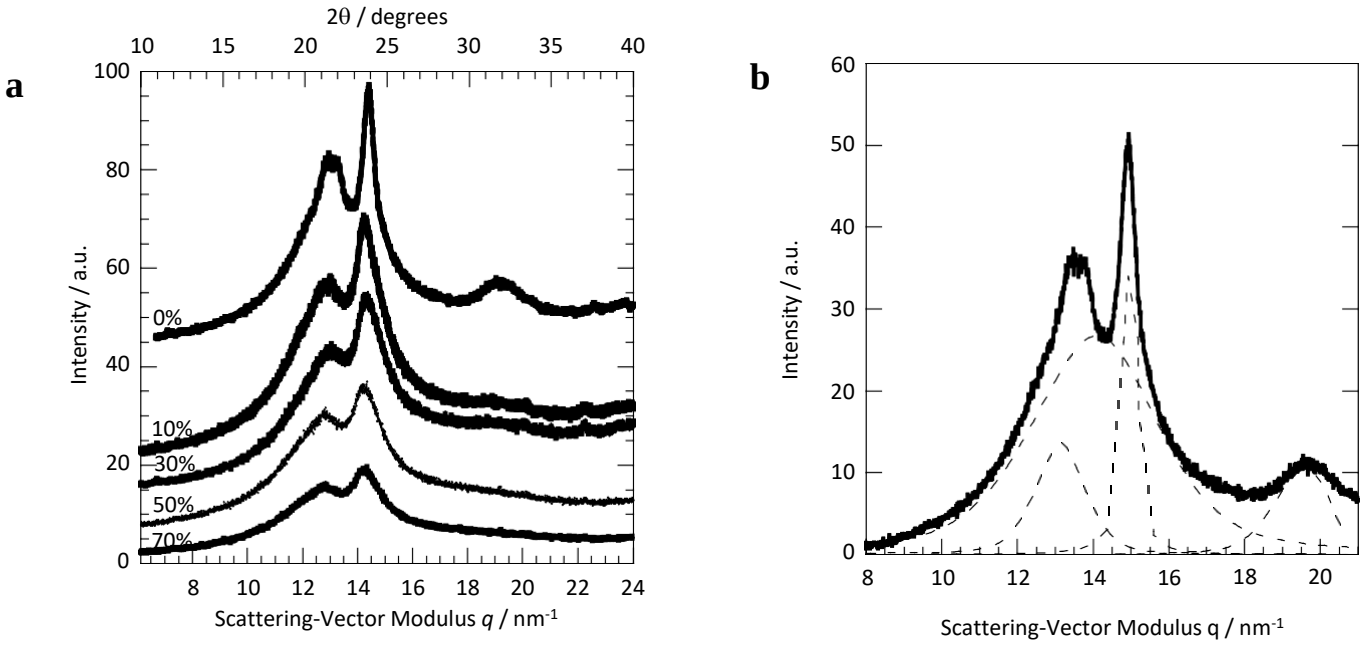

Figure 6. (**a)** WAXS diffractograms for several amount (wt.%) of particles, and **(b)** X-Ray profile of the PVdF-HFP membrane (solid line) with the resolved individual reflections (dashed lines).

The PVdF and the PVdF/HFP copolymers have been investigated through different studies to comprehend the influence of several parameters like blendings[56] with salts,[50] plasticizers,[50] fillers[57] or/and mechanical[56, 58] and treatment[59] effects on the obtained membranes.

The diffractogram of the membrane without fillers (Fig. 6a) reveals three main peaks at the diffraction angles 2θ = 20.8°, 23.3° and 31.3°, and a hump at 2θ = 21.7° due respectively to the crystalline and amorphous phases. The three crystalline peaks can be respectively

associated to the reflections (100)+(020), (110) and (021).[60] These peaks are representative of the coexistence of the β phase for the first peak and an orthorhombic crystal lattice of the copolymer in its form II (or α) for the two other peaks. According to the X-ray diffraction measurements shown in the Figure 6a, a crystalline phase remains with the fillers. The α phase crystals continue considering the peak positions of the different crystalline phases. Actually both persistent peaks, between 20 and 24°, are characteristic of the crystals of α and β phases . Their intensities decrease with the loading. Both contributions of amorphous and crystalline phases were separated as shown in the Figure 6b. The presence of a β phase is due to the use of DMF at 60°C for the casting of the membrane. Indeed the solvent dissolves a part of the original α phase that, during the evaporation at 60°C, crystallizes into the β phase.

Each one of the three crystalline peaks was fitted with a pseudo-Voigt function usually used in X-ray powder diffraction fitting procedures (Fig. 6b). The positions and the Full Width at Half Maximum (FWHM) are recorded (SI Tab. S3). The FWHM of a peak is influenced by three main factors: (i) the presence of deviations to the ideal lattice, (ii) the evolutions and heterogeneities in strains on the crystallites, and (iii) the size of the crystallites.

The position of the peak related to the amorphous phase ($2\theta_{am}$) dramatically shifts for the low loadings, and after the percolation of the fillers. The composition of the amorphous phase cannot change during these both events. Thus this shift, indicating a potential decrease of correlation lengths, could be due to the absorption of strains of the other constituents like the crystalline phase or the fillers. This variation is comparable to the one of the crystallinity index (w_{cr}) obtained by the ratio of the integrated crystalline scattering to the total scattering (see SI M3). The crystallinity of the polymer phase decreases with the increase of the filler amount (Fig. 7a).

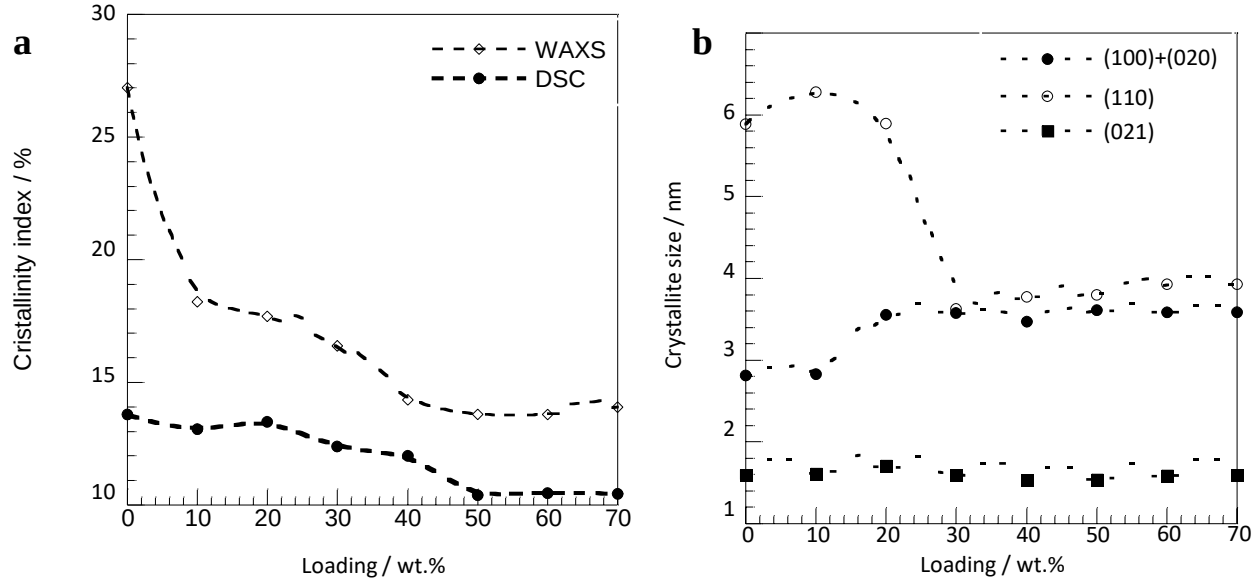

Figure 7. (a) Variation in the crystallinities obtained by DSC and WAXS, and **(b)** in the crystallite correlation lengths as a function of the filler content.

The crystallinity index obtained for the membrane with the neat copolymer is comparable to the crystallinity given by the supplier (25%). The comparison with the crystallinity obtained by DSC[30] shows a common trend. The gap of indexes can be due to the instrumental errors, the measurement theory, and the measurement protocol (DSC). The crystallinity index dramatically decreases for the low loadings, very slightly until the percolation, and a little bit more before reaching an asymptotic value from 50 wt.% upwards. To understand these trends, it is first interesting to compare the three crystallite sizes, obtained through the formula of Debye-Scherrer (see SI M4),[61] as a function of the loading (Fig. 7b). The characteristic size of the crystallites along the (021) reflection of the orthorhombic lattice is small and invariant. It characterizes the paracrystalline aspect of the crystal phase. In contrast to this invariance, the two other sizes drastically change at the percolation threshold, one varying from 6.0 to 3.8 nm and the other one from 2.8 to 3.6 nm (Fig. 7b). The paracrystal character is then reinforced.

The variation in *FWHM* can be also explained by a change of strains undergone by the crystallites. In addition, two phenomena are usually at the origin of the peak variation, the

very small size of the crystallites on the one hand, and a random distribution of crystalline parameters round the average value on the other hand.

Using this reasoning, before the percolation, both longer lengths are large and the crystallites under strain. And after the percolation these sizes shift to 3.5 nm and the strains become nil. Three main reasons can explain these evolutions: (i) with the loading, the crystallites are getting smaller, as a result the strain on one crystallite decreases, (ii) the amorphous phase absorbs a part of this strain, in agreement with a previous hypothesis, and (iii) in the process to obtain this membrane,[30] the membranes with a high loading contain a porosity which can also play the role of strain absorber.

The average volume of the crystallites can be obtained by the multiplication of the three main correlations lengths. This value gives an order of magnitude of its variation in the loading which also is the variation in the surface of the crystallites since the smallest length slightly varies. Taking into account both previous main inferences namely the constancy of the intercrystallite length, and the evolution of the strains in the membranes as a function of the loading, this trend can be interpreted. First of all, the continuum between the strains during the process to obtain the membranes, and in the final membranes is assumed. The following interpretation was put together in the light of Ostwald's ripening: (i) Before the percolation, the casting creating strains, the ripening is promoted, and the average volume significantly increases, and (ii) the small crystallites tend to disappear and the bigger ones to get larger. The distribution of average volumes becomes more monodisperse. At the percolation threshold, this average volume dramatically comes down following the variations in size of the crystallites (Fig. 7b). The homogeneity of the system during the casting permits to maintain the monodisperse character of this new distribution of smaller crystallites. This evolution is then due to the strains on the crystallites by the surrounding phase, i.e. the swelled aggregates of particles. At the percolation threshold, the particles therefore hinder the crystallisation. Beyond the percolation, the average volume slightly increases for two reasons: (i) the distribution is already well-nigh monodisperse, so the ripening is less important, and (ii) strains in the membranes do not exist, so the casting unfolds without strains. To sum up, with the loading, (i) the crystallinity index of the polymer phase decreases, (ii) the crystallites vary from a polydisperse population under light stress, in which the aggregates press the

polymer phase during the casting, to a monodisperse population without strain during the casting and in the obtained membranes.

Finally, a peak massif is observed (Fig. 4a) in the 2θ range going from 37 to 50° (between 22 and 30 nm^{-1}). This massif is not frequently described and attributed to the intrachain distances. In few diffractograms, three small broad peaks emerging from the massif stand out. They can be successively interpreted as the C-H, C-F and C-C distances.

Conclusions

The morphology, structure, crystallinity and internal interactions of nanocomposite electrolytic membranes have been described as a whole over a very large range of lengths (nm to Å). The particle aggregates ranged from 50 to 500 nanometers in size with radii of swelled particles around 13 nm. These aggregates are swelled in water creating an interaction with the polymer phase during the casting and in the obtained membranes. These membranes vary in two main regimes before and after the percolation threshold of the particles based upon the percent of particle loading. Before the threshold, the proton conductivity is low and the crystalline phase is under slight stress with a polydisperse population. After the threshold, the proton conductivity increases and the population of crystallites becomes monodispersed. In this system, the interdigitation of the sulfonated polystyrene shells could be at the origin of these behaviours. Indeed they locally act as strain regulators since it is a unifying hypothesis of the study.

This work permitted to incrementally underpin the elucidation of a multiscale complex structure. Beyond this constructive and unique insight, this overall comprehension gives the opportunity to better understand other close implied properties such as mechanical behaviours or transport mechanisms.

Acknowledgements

This research was supported by the PAN'H program through ANR MENHYR coordinated by H. Galiano then J. Bigarré from the CEA Le Ripault acknowledged for their help and work.

The authors thank C. Rochas and J. Jestin as local contacts respectively on the D2AM beamline at ESRF and the PAXE beamline at the LLB, S. Pouget for the fruitful discussions about WAXS, C. Cailleteau for support to realize the SEM micrographs and her valuable assistance, and M. Reback for his perusal.

Notes and references

[a] Univ. Grenoble Alpes, INAC-SPRAM, F-38000 Grenoble, France; CNRS, INAC-SPRAM, F-38000 Grenoble, France; CEA, INAC-SPRAM, F-38000 Grenoble, France. E-mail: manuel.marechal@cea.fr

[b] Univ. Grenoble Alpes, LEPMI, F-38000 Grenoble, France; CNRS, LEPMI, F-38000 Grenoble, France.

[c] LUNAM Univ., Université du Maine, CNRS UMR 6283, IMMM, département PCI, Avenue Olivier Messiaen, F-72085 Le Mans Cedex 9, France.

[d] CEA/DAM, Le Ripault, F-37260 Monts, France.

[e] Univ. Grenoble Alpes, F-38000 Grenoble, France; CEA, LITEN, F-38054, Grenoble, France.

Electronic Supplementary Information (ESI) available: [details of any supplementary information available should be included here]. See DOI: 10.1039/b000000x/

1. D. J. Jones and J. Roziere, *Adv. Polym. Sci.*, 2008, **215**, 219-264.
2. G. Alberti and M. Casciola, *Annu. Rev. Mater. Res.*, 2003, **33**, 129-154.
3. H. W. Zhang and P. K. Shen, *Chem. Rev.*, 2012, **112**, 2780-2832.
4. C. Laberty-Robert, K. Valle, F. Pereira and C. Sanchez, *Chem. Soc. Rev.*, 2011, **40**, 961-1005.
5. V. Ramani, H. R. Kunz and J. M. Fenton, *J Membrane Sci*, 2005, **266**, 110-114.
6. Y. S. Park and Y. Yamazaki, *Eur. Polym. J.*, 2006, **42**, 375-387.
7. P. Bebin, M. Caravanier and H. Galiano, *J Membrane Sci*, 2006, **278**, 35-42.
8. D. H. Jung, S. Y. Cho, D. H. Peck, D. R. Shin and J. S. Kim, *J. Power Sources*, 2003, **118**, 205-211.
9. F. Mura, R. F. Silva and A. Pozio, *Electrochim. Acta*, 2007, **52**, 5824-5828.
10. W. Lee, H. Kim, T. K. Kim and H. Chang, *J Membrane Sci*, 2007, **292**, 29-34.
11. C. Yang, S. Srinivasan, A. B. Bocarsly, S. Tulyani and J. B. Benziger, *J Membrane Sci*, 2004, **237**, 145-161.

12. C. S. Karthikeyan, S. P. Nunes, L. A. S. A. Prado, M. L. Ponce, H. Silva, B. Ruffmann and K. Schulte, *J Membrane Sci*, 2005, **254**, 139-146.
13. Y. Zhang, H. M. Zhang, Y. F. Zhai, X. B. Zhu and C. Bi, *J. Power Sources*, 2007, **168**, 323-329.
14. J. H. Chang, J. H. Park, G. G. Park, C. S. Kim and O. O. Park, *J. Power Sources*, 2003, **124**, 18-25.
15. J. D. Kim and I. Honma, *Electrochim. Acta*, 2003, **48**, 3633-3638.
16. R. A. Zoppi, C. R. deCastro, I. V. P. Yoshida and S. P. Nunes, *Polymer*, 1997, **38**, 5705-5712.
17. R. A. Vargas, V. H. Zapata, E. Matallana and M. A. Vargas, *Electrochim. Acta*, 2001, **46**, 1699-1702.
18. S. W. Li and M. L. Liu, *Electrochim. Acta*, 2003, **48**, 4271-4276.
19. K. Tadanaga, H. Yoshida, A. Matsuda, T. Minami and M. Tatsumisago, *Electrochem. Commun.*, 2003, **5**, 644-646.
20. Y. S. Kim, F. Wang, M. Hickner, T. A. Zawodzinski and J. E. McGrath, *J Membrane Sci*, 2003, **212**, 263-282.
21. B. Tazi and O. Savadogo, *J. New Mater. Electrochem. Syst.*, 2001, **4**, 187-196.
22. S. M. J. Zaidi, S. D. Mikhailenko, G. P. Robertson, M. D. Guiver and S. Kaliaguine, *J Membrane Sci*, 2000, **173**, 17-34.
23. R. H. He, Q. F. Li, G. Xiao and N. J. Bjerrum, *J Membrane Sci*, 2003, **226**, 169-184.
24. M. W. Park, J. C. Yang, H. S. Han, Y. G. Shul, T. H. Lee and Y. I. Cho, *Denki Kagaku*, 1996, **64**, 743-748.
25. J. A. Asensio, S. Borros and P. Gomez-Romero, *Electrochem. Commun.*, 2003, **5**, 967-972.
26. B. Tazi and O. Savadogo, *Electrochim. Acta*, 2000, **45**, 4329-4339.
27. B. Baradie, C. Poinsignon, J. Y. Sanchez, Y. Piffard, G. Vitter, N. Bestaoui, D. Foscallo, A. Denoyelle, D. Delabouglise and M. Vaujany, *J. Power Sources*, 1998, **74**, 8-16.
28. B. Bonnet, D. J. Jones, J. Roziere, L. Tchicaya, G. Alberti, M. Casciola, L. Massinelli, B. Bauer, A. Peraio and E. Ramunni, *J. New Mater. Electrochem. Syst.*, 2000, **3**, 87-92.
29. V. Di Noto, M. Piga, G. A. Giffin, E. Negro, C. Furlan and K. Vezzu, *ChemSusChem*, 2012, **5**, 1758-1766.
30. F. Niepceron, B. Lafitte, H. Galiano, J. Bigarre, E. Nicol and J. F. Tassin, *J Membrane Sci*, 2009, **338**, 100-110.
31. M. Marechal, R. Wessel, J. P. Diard, J. Guindet and J. Y. Sanchez, *Electrochim. Acta*, 2007, **52**, 7953-7963.
32. K. D. Kreuer, S. J. Paddison, E. Spohr and M. Schuster, *Chem. Rev.*, 2004, **104**, 4637-4678.
33. P. Zapata, D. Mountz and J. C. Meredith, *Macromolecules*, 2010, **43**, 7625-7636.
34. W. H. J. Hogarth, J. C. D. da Costa, J. Drennan and G. Q. Lu, *J. Mater. Chem.*, 2005, **15**, 754-758.
35. O. Sel, A. Soules, B. Ameduri, B. Boutevin, C. Laberty-Robert, G. Gebel and C. Sanchez, *Adv. Funct. Mater.*, 2010, **20**, 1090-1098.

36. K. Valle, P. Belleville, F. Pereira and C. Sanchez, *Nat. Mater.*, 2006, **5**, 107-111.
37. V. Maneeratana, J. D. Bass, T. Azais, A. Patissier, K. Valle, M. Marechal, G. Gebel, C. Laberty-Robert and C. Sanchez, *Adv. Funct. Mater.*, 2013, **23**, 2872-2880.
38. O. Sel, T. Azais, M. Marechal, G. Gebel, C. Laberty-Robert and C. Sanchez, *Chem. Asian J.*, 2011, **6**, 2992-3000.
39. C. Sanchez, C. Boissiere, S. Cassaignon, C. Chaneac, O. Durupthy, M. Faustini, D. Grosso, C. Laberty-Robert, L. Nicole, D. Portehault, F. Ribot, L. Rozes and C. Sassoye, *Chem. Mater.*, 2014, **26**, 221-238.
40. D. Truffier-Boutry, A. De Geyer, L. Guetaz, O. Diat and G. Gebel, *Macromolecules*, 2007, **40**, 8259-8264.
41. L. Rubatat, G. Gebel and O. Diat, *Macromolecules*, 2004, **37**, 7772-7783.
42. F. E. M. Obrien, *JSIPI*, 1948, **25**, 73-76.
43. J. C. Perrin, S. Lyonnard, A. Guillermo and P. Levitz, *J. Phys. Chem. B*, 2006, **110**, 5439-5444.
44. Y. S. Ding, S. R. Hubbard, K. O. Hodgson, R. A. Register and S. L. Cooper, *Macromolecules*, 1988, **21**, 1698-1703.
45. G. Carrot, A. El Harrak, J. Oberdisse, J. Jestin and F. Boue, *Soft Matter*, 2006, **2**, 1043-1047.
46. P. Debye and A. M. Bueche, *J. Appl. Phys.*, 1949, **20**, 518-525.
47. A. M. Bueche and P. Debye, *Phys Rev*, 1949, **75**, 1308-1308.
48. B. H. Zimm, *J. Chem. Phys.*, 1948, **16**, 1099-1116.
49. N. J. Wagner, R. Krause, A. R. Rennie, B. Daguanno and J. Goodwin, *J. Chem. Phys.*, 1991, **95**, 494-508.
50. S. Abbrent, J. Plestil, D. Hlavata, J. Lindgren, J. Tegenfeldt and A. Wendsjo, *Polymer*, 2001, **42**, 1407-1416.
51. F. Balta-Calleja and C. G. Vonk, *X-ray Scattering of Synthetic Polymers*, Elsevier, Amsterdam, 1989.
52. A. Guinier, *X-Ray Diffraction: In Crystals, Imperfect Crystals, and Amorphous Bodies*, Dover Publications, Toronto, 2013.
53. C. Cailleteau, F. Angeli, F. Devreux, S. Gin, J. Jestin, P. Jollivet and O. Spalla, *Nat. Mater.*, 2008, **7**, 978-983.
54. L. Rubatat, A. L. Rollet, G. Gebel and O. Diat, *Macromolecules*, 2002, **35**, 4050-4055.
55. P. Lindner and T. Zemb, eds., *Neutron, X-rays and light scattering: Introduction to an investigate tool for colloidal and polymeric systems.*, North Holland-Elsevier, Amsterdam, 1991.
56. C. H. Du, B. K. Zhu and Y. Y. Xu, *J. Mater. Sci.*, 2006, **41**, 417-421.
57. J. Buckley, P. Cebe, D. Cherdack, J. Crawford, B. S. Ince, M. Jenkins, J. J. Pan, M. Reveley, N. Washington and N. Wolchover, *Polymer*, 2006, **47**, 2411-2422.
58. X. J. He, K. Yao and B. K. Gan, *J. Appl. Phys.*, 2005, **97**, 1-6.
59. J. H. Cao, B. K. Zhu, G. L. Ji and Y. Y. Xu, *J Membrane Sci*, 2005, **266**, 102-109.
60. R. Hasegawa, Takahash.Y, H. Tadokoro and Y. Chatani, *Polym. J.*, 1972, **3**, 600-610.
61. L. E. Alexander, *X-ray diffraction methods in polymer science*, Wiley-Interscience, New York, 1969.

ARTICLE